Research Article

Effects of air swirler geometry on air and spray droplet interactions in a spray chamber

Shraddha Sharma(iD), **Kushal Ghate**(iD), **Thirumalachari Sundararajan**(iD) and **Srikrishna Sahu**(iD)

Abstract

In this work, interactions between cold spray and swirl airflow are characterized experimentally and numerically for various air swirler geometries. The number of vanes, vane angle, vane curvature, and air velocity are varied for the swirling airflow. Spray visualization and phase Doppler interferometry techniques have been employed to obtain important parameters such as spray cone angle and mean drop size. In the numerical work, the Realizable $k-\varepsilon$ turbulence model has been employed along with the Linearized Instability Sheet Atomization and Taylor Analogy Breakup to simulate spray field. The predicted results for the airflow field compare well with available experimental results in published literature. Good match is also found between the present predictions and measured spray data. The radial distribution of Sauter mean diameter exhibits peak values at the periphery of the spray near the injector, due to liquid swirl. The peak Sauter mean diameter shifts to the spray axis, beyond the recirculation zone, due to entrainment of droplets by the swirling air stream. The volume fraction of droplets exhibits multi-modal distribution, due to the interactions between spray droplets and recirculating airflow. A curved swirler gives rise to finer spray compared to a flat swirler, due to lower losses and better utilization of momentum.

Keywords

Recirculation, swirler geometry, spray air interaction, droplet entrainment, curved vanes

Introduction

Gas turbine engines are widely used in aircraft, liquid rocket engines, and so on for continuous power generation. Air swirler is mounted on the dome of gas turbine combustor for swirl generation and flame stabilization. The existence of swirl in a flow process creates a low-pressure zone near the axis, which, in turn, gives rise to the formation of a recirculation zone known as the Central Toroidal Recirculation Zone (CTRZ). Gas recirculation within a combustor increases the residence time of spray droplets and it also promotes mixing between the combustion products and spray droplets. The resultant increase in the rate of evaporation and heat availability improve the flame stability.[1] The intensity of swirl flow can be characterized by a swirl momentum based non-dimensional number known as Swirl Number (S_M).[2] It is defined as the ratio of the axial flux of angular momentum (G_ϕ) to the product of axial flux of the axial momentum (G_x) and the equivalent nozzle radius (R), as

Department of Mechanical Engineering, Indian Institute of Technology Madras, Chennai, India

Corresponding author:
Thirumalachari Sundararajan, Department of Mechanical Engineering, Indian Institute of Technology Madras, Chennai 600036, India.
Email: tsundar@iitm.ac.in

$$S_M = \frac{G_\phi}{G_x \times R} \qquad (1)$$

However, based on a geometric parameter of the annular swirler, for a constant vane angle α (degree), the geometric swirl number (S_G) is defined as

$$S_G = \frac{2}{3} \left\{ \frac{1 - \left(\frac{D_h}{D_t}\right)^3}{1 - \left(\frac{D_h}{D_t}\right)^2} \right\} \times \tan \alpha \qquad (2)$$

where D_h and D_t are the hub and tip diameters (mm) of the swirler geometry.

Swirling flows have been classified into weak swirling flows ($S_G < 0.3$) and strong swirling flows ($S_G > 0.6$), based on the geometric swirl number. In a strong swirling flow, the formation of CTRZ takes place due to the presence of large axial pressure gradients, but, in a weak swirling flow, the axial pressure gradients are insufficient to cause significant internal recirculation.[3] Gas recirculation creates a well-mixed zone of reactants and also improves mixing with hot products which serve as sources for heat and chemically active species.[4] Recirculation also enhances mixing by reducing the distance required for diffusion of fuel and air.[5]

Reddy et al.[6] experimentally investigated the flow field characteristics of a swirler in a combustion chamber. Apart from the CTRZ, the CRZ (Corner Recirculation Zone) and the PVC (Precessing Vortex Core) were also analyzed at a location far downstream of the swirler. Velocity fluctuations of high magnitude were observed in several planes, which indicated the high degree of turbulence generated by swirl. Raj and Ganesan[7] experimentally analyzed the flow through a 30° vane swirler and the CTRZ and CRZ were identified using a five-hole pitot probe. It was found that the length and width of recirculation zone depend on the amount of turbulence created by the swirler. Dang et al.[8] studied the influence of swirl number on isothermal and reacting flow fields. The length of CTRZ of reacting flows was found shorter than that of the non-reacting flows. However, the recirculation velocity, fluctuating velocity, and Reynolds shear stress components of reacting flows were observed to be larger. Kilik[9] experimentally investigated the effects of the vane outlet angle and the blockage ratio on the aerodynamic characteristics of the downstream recirculation region and the pressure drop through the swirlers by the use of four swirlers (two flat and two curved vanes). In general, curved vanes were found to operate much more efficiently than flat vanes. Larger and stronger recirculation region and higher pressure drop were observed with increase in blockage ratio. It was concluded that swirl number is not an all-inclusive parameter that can only be used to classify the effects of inlet swirl on flow field. The type, method of generation, and the distribution of inlet swirl profile also significantly contribute to the development of the flow field. Muthuselvan et al.[10] carried out a computational analysis of flow through an axial swirler for various swirl angles from 20° to 70° in steps of 10°. It was found that the length of CTRZ increases with swirl angle initially, but after 50°, it remains nearly constant. Khandelwal et al.[11] computationally examined the effects of the geometric parameters of swirler on the flow characteristics and the effect of mass flow on pressure drop coefficient. It was found that the axial reverse flow velocity, turbulence intensity, and the pressure drop increase with an increase in the vane angle. Yilmaz[12] numerically investigated the effect of swirl number on combustion characteristics such as temperature, velocity, and gas concentrations in a natural gas diffusion flame using computational fluid dynamics (CFD) fluent. The results indicated that the degree of swirl significantly affects the size of CTRZ and fluid dynamics behavior of natural gas diffusion flame.

Pressure-swirl atomizer (simplex atomizer) is widely used for spray generation in gas turbine engines, marine combustors, and industrial furnaces. In this atomizer, liquid is introduced through tangential ports to a central swirl chamber. The swirling liquid pushes against the wall of swirl chamber and develops a hollow air core. At the exit of the injector, a thin conical sheet is produced due to the swirl velocity of liquid. The interaction between thin liquid sheet and surrounding gas causes hydrodynamic instability of the liquid sheet and results in the formation of ligaments and droplets.[13]

Modern combustors adopt lean direct injection (LDI) strategy to achieve enhanced atomization and reduced emissions. LDI features a coaxially fitted swirler-atomizer assembly and direct injection of fuel and air into the combustor without any premixing. Since the fuel and air are not premixed, the performance of LDI heavily depends upon the design of the air swirler.[14]

Dunand et al.[15] experimentally investigated the influence of a swirling annular gas jet, momentum flux ratio, and surrounding pressure on the breakup and atomization of liquid jet. The results illustrated that low swirl causes slight enhancement in the atomization with no major changes, but the topology of flow changes significantly when a critical amount of rotational momentum is imparted to the gas stream. This transition leads to a significant decrease in liquid jet breakup length and an inversion of droplet distribution. Sanadi et al.[16] experimentally investigated the spray characteristics of a hollow cone spray in an unconfined, low-speed co-annular isothermal swirling air jet environment. A guided vane swirler with a vane angle of 45° (corresponding to $S_G = 0.8$) was used to impart swirling motion to the co-axial airflow. The results indicated that Sauter mean diameter (SMD) in the radial

direction is highly dependent on the swirling airflow interacting with the spray. The hollow cone tends to entrap the swirl stream, and swirling air causes fanning out of the spray droplets. Muthuselvan et al.[10] investigated the spray characteristics of 10 different configurations of small-scale simplex atomizers for cases with and without concentric swirl airflow using high-speed imaging and Malvern particle analyzer. Significant decrease in SMD value was observed with an increase in the swirl airflow rate, and high swirl airflow condition resulted in bimodal size distribution in the vicinity of the injector. De La Rosa et al.[17] investigated the effects of swirl number on the performance of a liquid spray in association with a flat vane axial swirler. It was concluded that flow reversal of the drops occurs at a high swirl number within the recirculation region. Also, the radial dispersal of drops increases with increase in swirl strength while the concentration of large drops increases near the core of the swirling field. Hadef and Lenze[18] experimentally investigated the effect of two swirl configurations, co- and counter-swirling, on the behavior of droplets in a spray flame formed by two swirling annular jets. The results indicated that the counter-swirl configuration causes finer and more spatially dispersed atomization, though SMD values vary little with the change in direction of swirl. Rajamanickam and Basu[19] experimentally investigated near-field breakup and interaction of a hollow cone liquid sheet with co-annular swirling airflow. Flapping induced breakup due to strong vortices was mentioned as a unique characteristic of swirling flow. The weak, critical, and strong-interaction zones between liquid and gas phases were presented as functions of the momentum ratio (MR). Kelvin Helmholtz waves were observed to cause the breakup in the strong-interaction zone, whereas, in the weak-interaction zone, the breakup was expected to be surface tension driven.

It is evident from the literature survey presented above that significant amount of work has been carried out on the structure of airflow from a swirler and its interactions with the liquid spray, in a combustor. Still, there is a need to characterize the effects of air swirler geometry on swirl airflow development and the resulting axial and radial drop size distributions within spray chamber, in detail. This will be helpful to identify the optimal swirler geometry which will aid in obtaining fine spray atomization as well as desired droplet size distribution.

This study deeply examines the structure of recirculating flow and spray–airflow interactions for different air swirler geometries. The airflow Reynolds number (Re_a) for these studies lies in the range of 1×10^4 to 2×10^5. The modified Weber Number, We^* ($= (P_{inj} \times d_o)/\sigma$), ranges from 4×10^3 to 3.4×10^4 and the geometric swirl number (S_G) range for the airflow field is 0.4–1.4. The study involves both computational and numerical work. Computational analysis is first
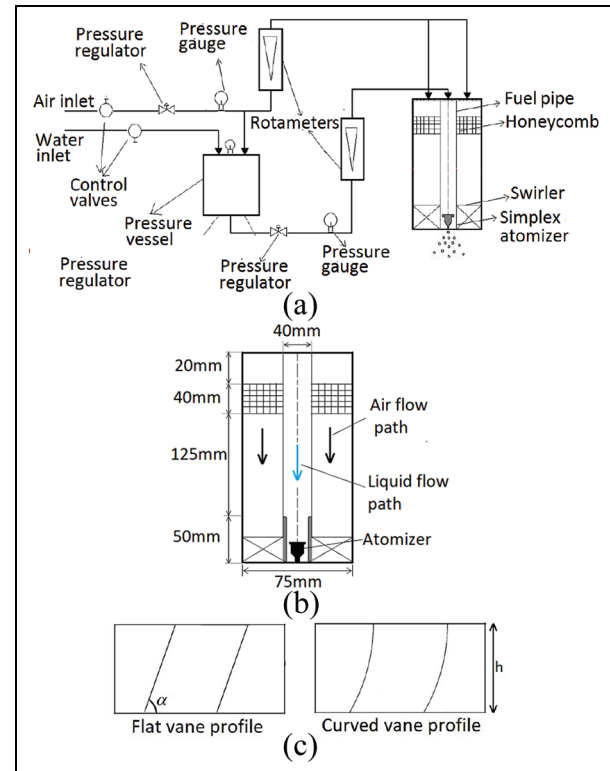

Figure 1. Schematic of experimental setup and swirler: (a) schematic of experimental setup, (b) enlarged view of test section, and (c) schematic of swirler.

performed to highlight the effect of the vane angle and vane number on the size of recirculation zone and associated airflow field characteristics. Subsequently, the simulated results on the effect of air swirler geometry on spray characteristics of hollow cone sprays are considered. In-house experimental data on the visualization of spray structure and droplet size distribution are presented to validate the results predicted by the numerical simulations. High speed shadowgraphy is used for spray visualization, and Phase Doppler Interferometer (PDI) is used for the evaluation of SMD and droplet size distribution. The numerical and experimental results discussed here provide a good understanding of the spray–swirl air interactions, and these will provide useful data for the development of optimal air swirlers.

Methodology

Experimental methodology

An experimental study is conducted to investigate the performance of swirler shape (flat and curved vanes) on the spray characteristics in a coaxially fitted swirler-atomizer assembly. Figure 1(a) represents the schematic of the experimental setup with all the pipeline

Table 1. Important dimensions of atomizer.

Parameter	Value
Orifice diameter	1 mm
Swirl chamber diameter	4.4 mm
Tangential port diameter	0.8 mm
No. of tangential ports	3
Atomizer constant (K)	0.3427

connections, Figure 1(b) represents the detailed dimensions of the test setup, and Figure 1(c) represents the elaborated swirler configuration. The swirlers consist of eight vanes with hub diameter of 41 mm, tip diameter of 75 mm, and vane thickness of 2 mm. The vane angles (α) of the swirler used are 30°, 45°, and 60° which give rise to geometric swirl number values of 0.46, 0.80, and 1.38, respectively. The height of the swirler varies from 20.2 to 35 mm depending upon the vane angle of the swirler. The profile of the curved vane is a circular arc in which the vane stagger angle is half of the vane outlet angle and the incidence angle is zero. The spray is generated by a pressure swirl atomizer (simplex atomizer). Important dimensions of atomizer are listed in Table 1.

Experiments are carried out at isothermal conditions using air and water as working fluids. Water flow rate is kept constant (0.949 L/m) by maintaining the injection pressure of 3 bar throughout the experiment, whereas the airflow rate is varied from 0 to 2000 L/m in steps of 500 L/m. A honeycomb is used upstream of the swirler to straighten the incoming airflow. Water is supplied at the required rate from a pressurized tank. Calibrated rotameters are used to measure air and water flow rates within an estimated accuracy of $\pm 1\%$ and $\pm 1.5\%$, respectively.

High-speed shadowgraphy is employed to capture spray images, using the high-speed camera and lamp arrangement shown in Figure 1. A PCO Dimax high-speed camera is employed to capture spray images using a LED source and diffuser plate at the rate of 7000 fps. The window size chosen is 60×60 mm. The images are processed by ImageJ software to get the variation of spray cone angle (θ).

A PDI (Artium PDI) is used to analyze the effect of swirling air on spray droplet size. Figure 2 shows the arrangement of PDI and experimental setup. The coherent laser beams emitted from the transmitter intersect and form a measurement probe volume. The transmitter is placed at an angle of 30° off the axis from the laser intersection point. The transmitter and receiver are placed at 500 mm distance from the probe volume. Particles passing through the probe volume scatter light that is collected by the receiver lens. A single aperture is used in the receiver to allow only light scattered by particles crossing a small region of the beam intersection
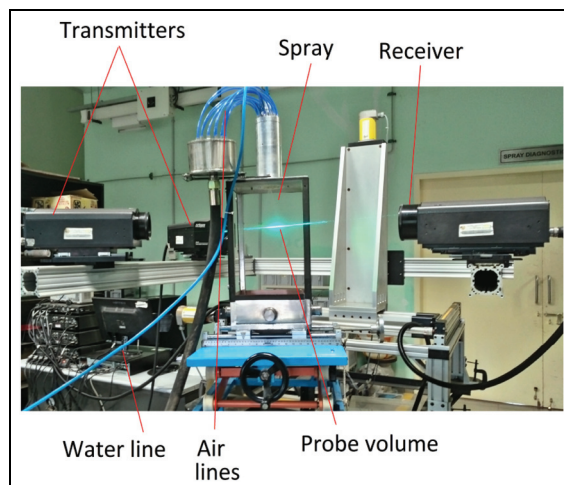
Figure 2. Phase Doppler Interferometry arrangement with experimental setup.

zone to reach the photodetectors. The fringe pattern is monitored regularly to avoid any error in the measurement, and channel validation of 90%–99% is achieved in every set of readings. Droplet behavior is captured at various axial and radial locations with the help of a traverse attached to the experimental setup.

Numerical methodology

Numerical simulations have been carried to analyze the effect of swirler geometry on the airflow field and spray structure. For validating the airflow field results, the geometry employed in the work of Raj and Ganesan[7] has been considered for the numerical simulation study, and the schematic of computational domain (D1) is shown in Figure 3(a). Another computational domain (D2) shown in Figure 3(b) is also used for simulating the spray–swirl air interaction, and this domain is similar to the spray geometry used in the present experimental study. The swirler geometry, with varying vane angle (30°, 45°, 60°), varying vane number (4, 6, 8, 10, 12), and different swirler profiles (flat and curved), is created in SolidWorks and exported to the CFD solver (Fluent 14.5) for meshing and post-processing. Three-dimensional tetrahedral meshing is adopted to take care of the shape complexities and also to reduce the mesh skewness. Cells are refined in critical regions like the swirler inlet and exit, in anticipation of high velocity and pressure gradients at these zones.

For simulating the airflow field, a pressure-based solver with velocity inlet boundary condition and first-order implicit transient formulation are used to solve the Navier–Stokes equations with source terms due to the presence of spray droplets. The SIMPLEC (Semi-Implicit Method for Pressure-Linked Equations-Consistent) scheme is used for pressure/velocity
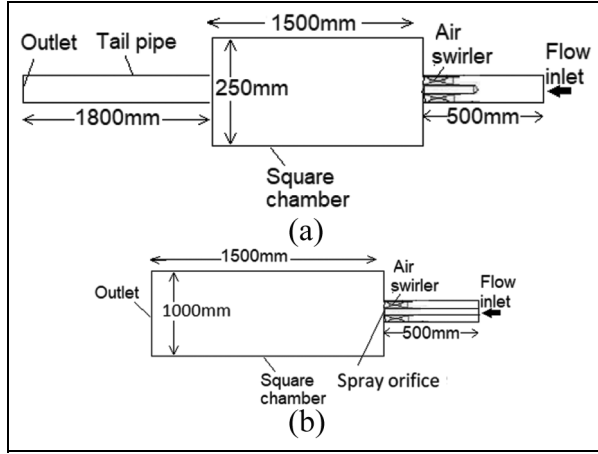
Figure 3. Schematic of computational domains: (a) schematic of computational domain (D1) for airflow field validation and (b) schematic of computational domain (D2) for spray–swirl air interaction study.

coupling for the airflow field simulation. Turbulence is modeled using the Realizable $k-\varepsilon$ model with standard wall functions. Realizable $k-\varepsilon$ model is known to exhibit superior performance for flows involving rotation and recirculation.[20]

The Eulerian–Lagrangian approach is employed for modeling the two-phase flow. Isothermal, non-evaporative situation corresponding to a water spray interacting with swirl air at ambient conditions is modeled here, and hence, the energy equation is not considered. Based on the LISA (Linearized Instability Sheet Atomization) model of Schmidt et al.,[21] a pressure swirl atomizer is modeled to inject droplets in terms of 200 particle streams. It was found that 200 particle streams are adequate to represent the initial distribution of droplets well. The LISA model is divided into two stages, involving initial film formation and subsequent sheet breakup and atomization, to model the primary breakup of the liquid jet. Droplets formed as per the LISA model are injected from the orifice, along with the swirling component of velocity. The TAB (Taylor Analogy Breakup) model which is based on Taylor's analogy[22] is used to simulate secondary breakup. This model employs the analogy between a distorting droplet and a spring mass-damper system. The restoring force on the mass is similar to the surface tension force, the external force on the mass is analogous to the superposition of the hydrodynamic impact and aerodynamic forces, and the damping force is due to liquid viscosity. The TAB model is recommended for low-Weber-number injections and is well suited for low-speed sprays at atmospheric pressure. The trajectory of a discrete phase liquid particle (or droplet) is predicted by integrating the force balance on the particle, which is written in a Lagrangian reference frame. This force balance equates the particle inertia with the forces acting on the particle, and can be written (for the x direction in Cartesian coordinates) as

$$\frac{du_l}{dt} = F_D(\bar{u} - u_l) + \frac{g_x(\rho_l - \rho_a)}{\rho_l} + F_x \quad (3)$$

where $\bar{u}$ is air phase velocity (m/s), u_l is the velocity of liquid (m/s), $F_D(\bar{u} - u_l)$ is the drag force per unit liquid mass, and F_x is additional acceleration term. The coefficient F_D is given by the equation

$$F_D = \frac{18\mu C_D Re_l}{\rho_l d_l^2 24} \quad (4)$$

In the above expression Re_l is the relative Reynolds number based on relative velocity between the drop velocity and gas flow. Also, droplet diameter is the length scale used for evaluating the Reynolds number. The drag coefficient, C_D, can be expressed as

$$C_D = \frac{24\left(1 + b_1 Re_l^{b_2}\right)}{Re_l} + \frac{b_3 Re_l}{b_4 + Re_l} \quad (5)$$

where $b_1 = exp(2.3288 - 6.4581\phi + 2.4486\phi^2)$, $b_2 = 0.0964 + 0.5565\phi$, $b_3 = exp(4.905 - 13.8944\phi + 18.4222\phi^2 - 10.2599\phi^3)$, and $b_4 = exp(1.4681 + 12.2584\phi - 20.7322\phi^2 + 15.8855\phi^3)$.

The above relations are adopted from the work of Haider and Levenspiel.[23] The particle shape factor, ϕ, is defined as the ratio of the surface area of a sphere having the same volume as the droplet and the actual droplet surface area.

Since the model needs the specification of the cone angle, a value of 30° has been specified which lies in the range of cone angle (27.5°–35°) measured in the present experiments. The physical and transport quantities are taken corresponding to isothermal water droplets injected into air at 1 bar and 298 K. The property values considered for the air and water media are as follows: air density ($\rho_a = 1.225$ kg/m^3), air viscosity ($\mu_a = 1.7394 \times 10^{-5}$ kg/ms), and water density ($\rho_l = 998.2$ kg/m^3), where subscripts "a" and "l" correspond to air and water, respectively.

Transient simulations are first carried out using the SIMPLEC scheme, until a steady flow is obtained. The DPM model is then enabled to inject the droplets at the required velocity (including swirl component) and initiate interactions between the discrete (spray droplets) and continuous (swirling air) phases. Unsteady particle tracking with a time step of 0.001 s is chosen to model droplet motion. For every discrete particle motion (DPM) updating, the continuous phase data are updated for 10 iterations. The boundary conditions imposed on the airflow field and spray droplets at the orifice (Figure 3(a)) are summarized in Table 2. Conditions studied are tabulated in Table 3.

Table 2. Input data for the simulation.

Conditions	Value
(a) Air flow data	
Inlet air velocity	15–30 m/s
Flow direction	Normal to swirler boundary
Inlet hydraulic diameter	107 mm
Inlet turbulence intensity	1%
Pressure outlet	Zero gauge pressure
Walls	Adiabatic, No-slip
(b) Spray input data	
Number of particle streams	200
Flow rate	0.006667 kg/s
Upstream pressure	800,000 Pascal
Injector inner diameter	3 mm
Pressure outlet	Zero gauge pressure
Spray half angle	30°

Grid independence test and validation of airflow field predictions

For ensuring grid independence of numerical results, the predicted maximum reverse velocity values for different grids are compared. The values are extrapolated to zero grid size (h → 0) by fitting fourth-order polynomial functions. These zero grid size extrapolations for the maximum reverse velocity are denoted as $V_{rev,e}$ (or "exact" reverse velocity). It is now possible to define the errors in the predictions of maximum reverse velocity as $\Delta V_{rev} = V_{rev,e} - V_{rev}$ for any non-zero grid size (h). The percentage reduction in relative error for the maximum relative velocity with respect to reduction in grid size is shown in Table 4. The relative errors for ΔV_{rev} become of the order of 1% (with respect to the

Table 3. Conditions studied in experiment and theory.

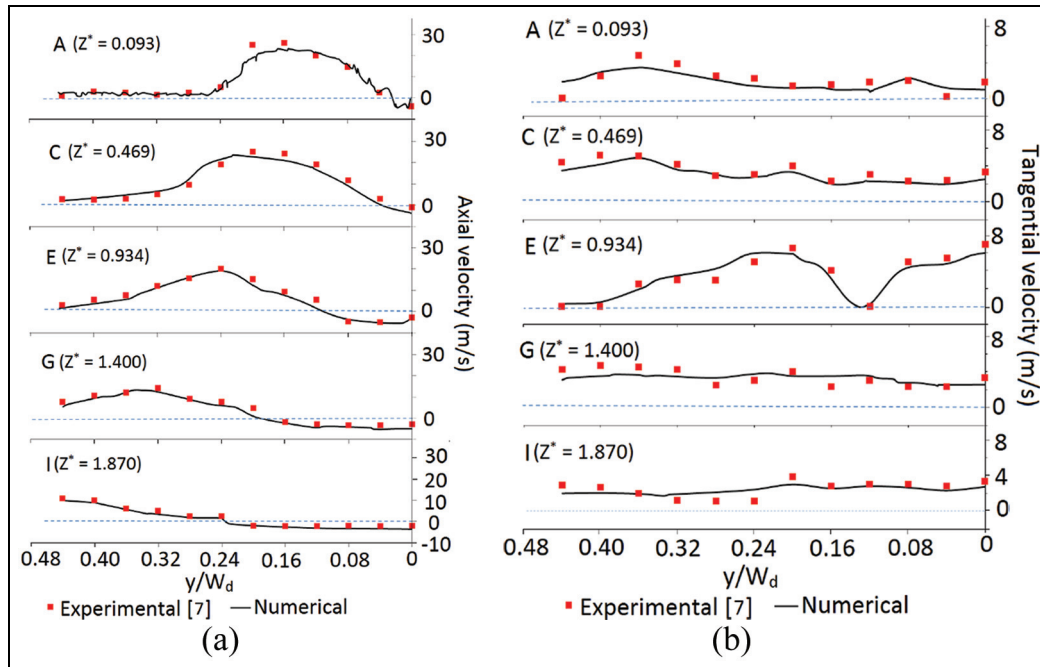| S. no.	Present study	D_h (mm)	D_t (mm)	d_0 (mm)	Liquid flow rate (L/m)	Air flow rate (L/m)	Re_a	Re_l	We^*	S_G
(Experimental/Numerical)										
1	Numerical	32	107	3	0.4	6829–13,658	1.01×10^5–2.03×10^5	7933	32,967	0.41, 0.71, 1.23
2	Both	41	75	1	0.949	0–2000	1.21×10^4–4.86×10^4	24,627	4121	0.46, 0.80, 1.38

Figure 4. Validation of computational predictions with available experimental data[7] for airflow simulation in domain D1 ($Re_a = 1.35 \times 10^5$, $S_G = 0.41$, $Z^* = z/D_t$), number of vanes = 8, $\alpha = 30°$: (a) radial profiles of axial velocity at different axial locations (A–I) and (b) radial profiles of tangential velocity at different axial locations (A–I).

Table 4. Grid independence data.

Grid index	No. of nodes	Normalized mesh size ($h/h_{initial}$)	$\Delta V_{rev}/V_{rev,\,e}$ (%)
G1	351,985	1	6.87
G2	426,778	0.9386	3.20
G3	532,985	0.8727	1.98
G4	722,172	0.7833	1.22
G5	914,584	0.7285	0.91

extrapolated zero grid solution) when grid 4 (G_4) and grid 5 (G_5) are employed. Therefore, G_4 has been used in all the subsequent simulations, keeping the computational economy in mind. The results have been converged below a tolerance level of 1×10^{-7} for all the computations.

In order to validate the numerical prediction for airflow without spray, the geometry (domain D1) adopted from the work of Raj and Ganesan[7] is considered. Measurements of axial and tangential components of velocities for this geometry are available for every 10 mm radial distance at various z/D_t axial stations downstream of the swirler. Some of these data are used to validate the velocity predictions of the present numerical simulations. The velocity components predicted at different axial planes Z^* (axial distance z is normalized by D_t; the diameter of blade tip 107 mm) are compared with the experimental results of Raj and Ganesan[7] in Figures 4(a) and (b). The experimental values are represented by discrete symbols and solid lines represent numerical results. A good agreement is observed between the experimental and computational results for all the axial locations considered. In fact, the differences are well within the reported experimental error of $\pm 5\%$. It is noted in passing that other turbulence models such as Standard k$-\varepsilon$, RNG k$-\varepsilon$, and so on were also attempted, but they did not give as good a comparison with experimental data as the Realizable k$-\varepsilon$ model adopted in this work.

Results and discussions

Imparting swirl to the air stream generates a large CTRZ wherein spray droplets are entrained, thereby providing an adequate residence time for liquid fuel evaporation and combustion. The presence of swirl in the airflow also increases the radial spread of the fuel spray because of centrifugal force. Furthermore, air swirl also contributes to higher velocity gradients, which promote the generation of turbulence and greater mixing between the reactants and products. Modification of air swirler geometry is expected to cause significant changes in the recirculation zone size, air velocity field, droplet breakup and dispersal, and
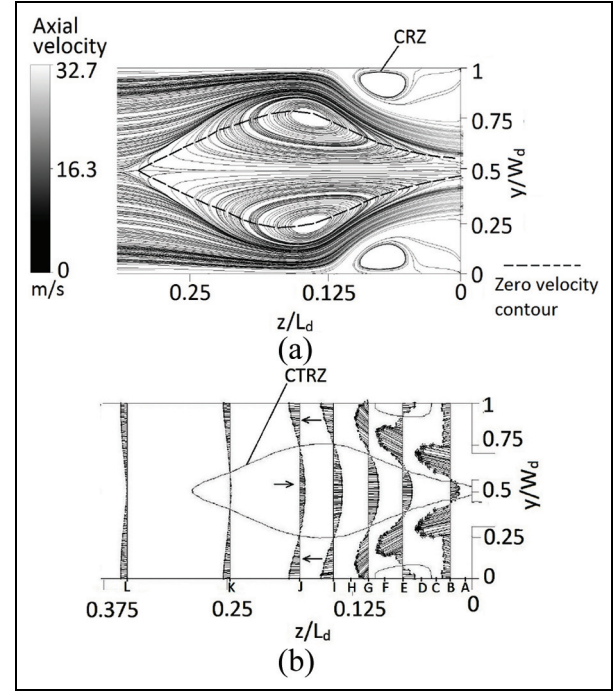

Figure 5. Air flow field in the combustor for a swirler with eight vanes and 30° vane angle ($Re_a = 1.35 \times 10^5$, $S_G = 0.41$): (a) streamlines and (b) axial velocity vectors ($V_{a\max} = 23.85$ m/s).

the mixing between the reactant species and products. In this section, the effects of swirler geometry on the airflow field are discussed first, followed by the interactions between swirling air and fuel spray droplets for a spray not undergoing evaporation or combustion (water spray in air).

Numerical predictions for the effects of swirler geometry on airflow field (D1)

Air flow structure and validation. Numerical simulations of airflow have been carried out for different flat vane swirler geometries, with number of vanes and swirl angle varied in a systematic way. Before presenting the effects of swirler geometry, some basic predictions concerning the airflow field structure are presented.

Initially, flow through a 30° swirler with eight vanes is analyzed, corresponding to a swirl number (S_G) of 0.41. Figure 5(a) represents the streamlines on the mid-plane (colored by axial velocity magnitude), showing the development of CTRZ and CRZ. The corresponding axial velocity vectors are shown in Figure 5(b). The CTRZ is identified by the location of points where the velocity magnitude becomes zero as shown in Figure 5(a) and (b). Inside the recirculation region, negative values of velocity are observed near the axis (Figure 5(b)), while outside the recirculation region, axial velocity values are positive and high in magnitude. The

Table 5. Effects of vane number and vane angle of swirler on airflow field parameters.

	Flow conditions	Length of recirculation zone (LRZ/L_d)	Width of recirculation zone (WRZ/W_d)	Maximum turbulent intensity (TI_{max}) (%)	Maximum reversal velocity (V_{rev}) (m/s)	Pressure loss factor (PLF)
Vane number	4 ($Re_a = 1.38 \times 10^5$, $S_G = 0.41$)	0.26	0.53	34.17	6.03	3.01
	6 ($Re_a = 1.37 \times 10^5$, $S_G = 0.41$)	0.27	0.53	34.83	6.37	3.17
	8 ($Re_a = 1.35 \times 10^5$, $S_G = 0.41$)	0.28	0.56	35.28	6.45	3.32
	10 ($Re_a = 1.33 \times 10^5$, $S_G = 0.41$)	0.28	0.55	35.96	6.683	3.54
	12 ($Re_a = 1.32 \times 10^5$, $S_G = 0.41$)	0.29	0.54	37.22	7.02	3.78
Vane angle	30° ($Re_a = 1.35 \times 10^5$, $S_G = 0.41$)	0.28	0.56	35.28	6.45	3.32
	45° ($Re_a = 1.35 \times 10^5$, $S_G = 0.71$)	0.64	0.66	45.01	9.93	8.76
	60° ($Re_a = 1.35 \times 10^5$, $S_G = 1.23$)	0.73	0.76	61.62	13.25	25.69

CTRZ is required for the stabilization of the flame whereas CRZ could give rise to emissions such as NO_x due to the formation of local hot spots.[24] Over the recirculation zone, axial velocity vectors are superimposed and a clear view of flow reversal within the recirculation zone is observed in Figure 5(b). In particular, the reverse flow region with small velocity magnitude is critical with respect to flame stability. The reverse flow is generated as a consequence of the low-pressure region occurring close to the axis, because of the swirl airflow. For the swirl angle of 30° ($S_G = 0.41$) considered here, the CTRZ occupies about 30% of spray chamber length. The reverse flow also plays an important role in the formation of the air core, which aids in hollow cone spray development. It is interesting to note that the air stream is directed radially outward (Figure 5(b)) near the injector, due to the presence of CTRZ. Such radial diversion is likely to facilitate droplet dispersal in the radial direction.

Characterization of swirling airflow field. The effects of air swirler geometry on the essential flow parameters are presented in Table 5. It is evident that the non-dimensional length and width of the recirculation zone, turbulent intensity, maximum reversal velocity magnitude, and pressure loss gradually increase with the number of vanes. Such increases can be attributed to the higher blockage caused by increase in the number of vanes. The high sensitivity of all the flow parameters with respect to variation in vane angle is clearly seen in Table 5. In particular, the size of recirculation zone, turbulence intensity, and pressure loss increase sharply with an increase in the vane angle. The pressure loss factor, which is a measure of the flow resistance offered to the air stream when it passes through the swirler, is defined in terms of the total pressure loss ($P_{01} - P_{02}$) as

$$PLF = \frac{P_{01} - P_{02}}{0.5\rho U_o{}^2} \quad (6)$$

where P_{01} and P_{02} are inlet and exit stagnation pressure (Pa) of air swirler and U_a is inlet air velocity (m/s).

Table 6 presents the variation in the length of CTRZ and the maximum turbulent kinetic energy (k_{max}) at different airflow Reynolds numbers (Re_a) for flat vane swirlers having 30°, 45°, and 60° vane angle values. Here, Re_a has been changed by varying the average inlet air velocity. The dimensionless length of CTRZ is found to be constant at all Re_a values, indicating the independence of recirculation zone size on inlet air velocity (Table 6). In fact, the recirculation zone width is also independent of the inlet air velocity (not shown in table).

For a fixed swirler geometry, when the inlet air velocity is changed, all velocity components change in the same proportion, resulting in the same recirculation

Table 6. Effects of air Reynolds number (Re_a) on airflow field parameters.

Air Reynolds number (Re_a)	$30^°$ swirler($S_G = 0.41$)		$45^°$ swirler($S_G = 0.71$)		$60^°$ swirler($S_G = 1.23$)	
	LRZ/L_d	$k_{max}(m^2/s^2)$	LRZ/L_d	$k_{max}(m^2/s^2)$	LRZ/L_d	$k_{max}(m^2/s^2)$
1.01×10^5	0.282	28.78	0.643	49.31	0.729	90.44
1.35×10^5	0.282	49.47	0.643	81.07	0.729	169.57
1.69×10^5	0.282	77.66	0.643	138.45	0.729	254.16
2.03×10^5	0.282	114.15	0.643	199.79	0.729	367.38
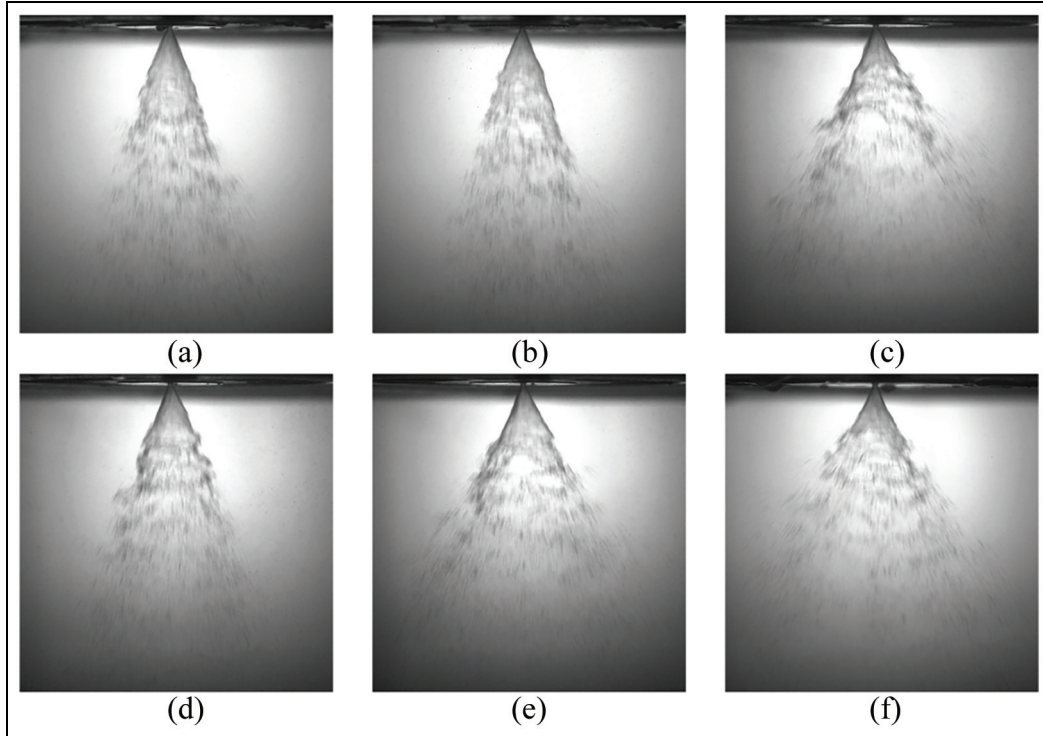
Figure 6. Spray images ($Re_a = 4.86 \times 10^4$, $Re_l = 2.46 \times 10^4$, $We^* = 4121$): (a) $30f$ ($S_G = 0.46$), (b) $45f$ ($S_G = 0.80$), (c) $60f$ ($S_G = 1.38$), (d) $30c$ ($S_G = 0.46$), (e) $45c$ ($S_G = 0.80$), and (f) $60c$ ($S_G = 1.38$).

zone size. The recirculation zone dimensions are strong functions of the swirl angle (or swirl number). Turbulent kinetic energy (k_{max}) is the energy content of eddies in turbulent flow. It is observed that the value of k_{max} increases approximately in proportion to the square of the inlet velocity (or Re_a), as expected.

Results of spray visualization (in-house experimental)

Variation of spray cone angle (θ). The initial angle of conical sheet formed at the nozzle exit is known as spray cone angle (θ). Spray cone angle governs the dispersion of spray, and good dispersion is required for rapid mixing of liquid with surrounding gas and also to get higher evaporation rate. Figure 6(a)–(f) represents the instantaneous images of spray for 30°, 45°, and 60° (flat and curved) swirlers; "*f*" and "*c*" denote flat and curved vane swirlers.

The steps followed for accurate measurement of spray cone angle are (1) averaging of 100 images, (2) background subtraction, and (3) edge detection. The processed image is shown in Figure 7(a). Figure 7(b) represents the spray cone angle variation with airflow rate for different swirlers.

The cone angle is measured at 20 mm downstream of the swirler exit and threshold value of 10% of maximum intensity is used to identify the spray edge. It is observed that the spray cone angle increases with airflow rate, and a wider dispersion is obtained for curved vane swirler as compared to that of flat vane swirler. The spray cone angle increases with increase in vane angle because higher swirl intensity is imparted to the flow. The radial
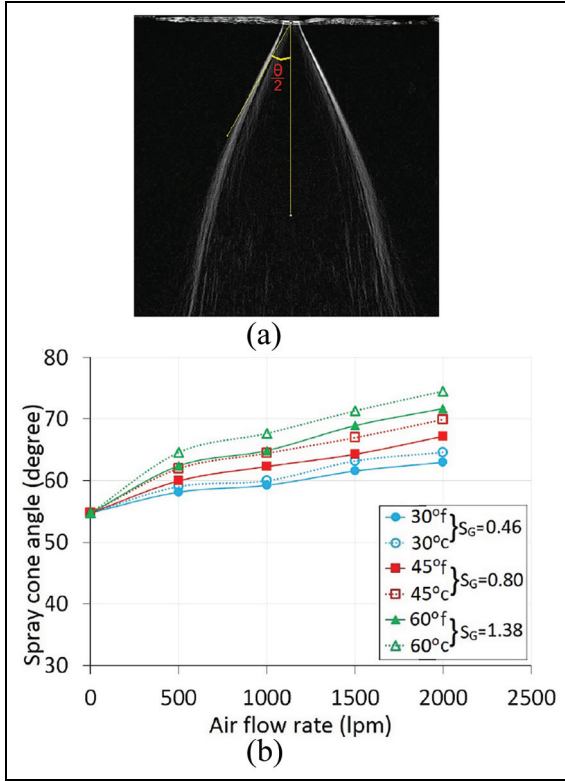
Figure 7. Spray cone angle (θ) variation with airflow rate ($Re_l = 2.46 \times 10^4$, $We^* = 4121$): (a) processed image and (b) spray cone angle versus airflow rate.

dispersion of spray increases due to higher centrifugal force associated with higher swirl. The use of curved vanes provides smooth guidance to the flow which reduces the tendency for flow separation; whereas in the case of flat vane swirler, the chances of flow separation are high. The use of curved vane swirler results in less pressure losses, and therefore, enhancement in spray

cone angle is obtained. Moreover, faster sheet breakup with smaller breakup length, larger spray dispersion, and enhanced secondary breakup are observed when curved vane swirler is used.

Droplet behavior in swirling air

Radial variation of SMD at different axial planes (D1). The SMD (or d_{32}) is a measure of the overall surface area of the fluid being sprayed for a given volume, which is very useful for processes involving evaporation. It is defined as the mean diameter of spray droplet with the same ratio of volume to surface area as the entire spray[25]

$$SMD \, or \, d_{32} = \frac{\sum_{i=1}^{N} n_i d_i^3}{\sum_{i=1}^{N} n_i d_i^2} \tag{7}$$

where n_i represents the number of droplets and d_i represents the mean diameter of droplets in the ith diameter range.

Also, since droplet breakup depends on the Weber number of the flow situation, a modified Weber number (We^*) based on the injection pressure is defined as

$$We^* = \frac{P_{inj} \times d_o}{\sigma} \tag{8}$$

where P_{inj} is the injection pressure, d_o is the orifice diameter, and σ is the surface tension of the liquid injected into air.

Figure 8(a) and (b) represents the evolution of the radial SMD variation along the axial direction (z/$L_d = 0.233$–0.666 identified as plane I, II, III, and IV, respectively). Radial variations of local SMD at various axial distances are plotted to understand the effect of
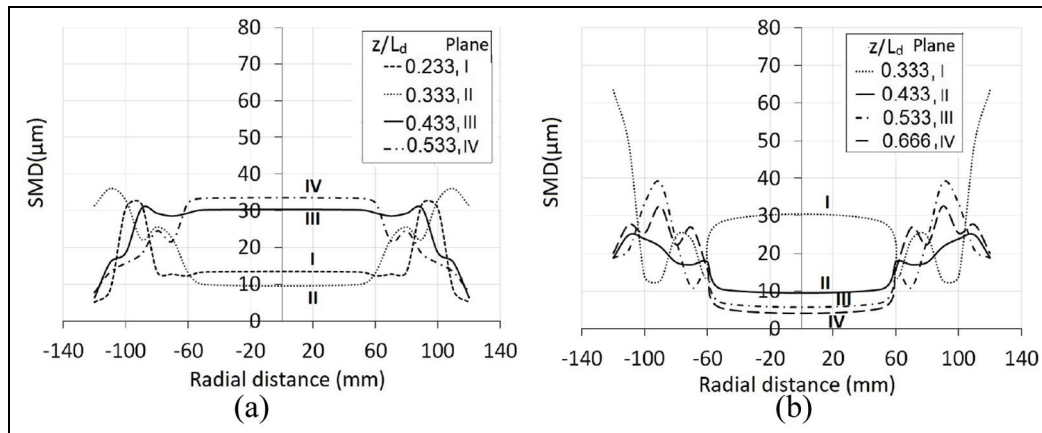

Figure 8. Effect of recirculation on radial variation of SMD at different axial distance ($Re_a = 1.35 \times 10^5$, $Re_l = 7.93 \times 10^3$, $We^* = 32967$): (a) 30° swirler ($S_G = 0.41$) and (b) 60° swirler ($S_G = 1.23$).
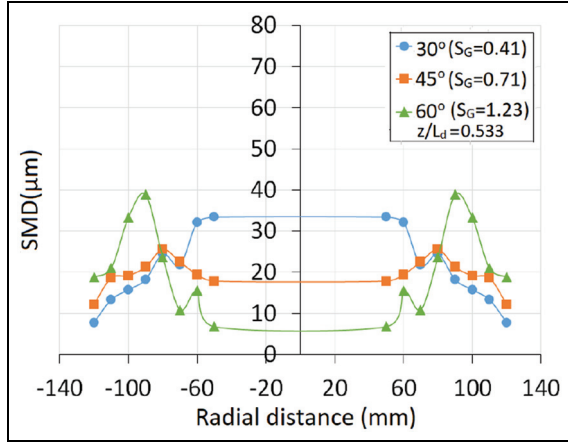
Figure 9. Radial variation of SMD for all swirlers ($Re_a = 1.35 \times 10^5$, $Re_l = 7.93 \times 10^3$, $We^* = 32967$, $z/L_d = 0.533$).

Figure 10. Schematic of spray.

recirculation zone on the spray distribution. The recirculation zone lengths for 30° and 60° swirlers are 423.15 mm ($z/L_d = 0.282$) and 1094.7 mm ($z/L_d = 0.729$), respectively. In the case of 30° swirler, peaks in droplet size are observed in the jet periphery region at planes closer to the injector (at $z/L_d = 0.233$ and 0.333). Smaller drop sizes occur close to the axis, since they are entrained by the reverse flow of air, due to the strong air recirculation. At higher axial distances corresponding to locations outside of the recirculation zone, larger droplets occur on the axis; it is evident that the forward stream of the recirculatory flow carries larger droplets toward the axis, while the reverse flow near the axis entrains smaller droplets and carries them back toward the injector. This idea is strengthened by the radially inward movement of the peak locations between the axial planes (z/L_d) at 0.233 (plane I) and 0.533 (plane IV). There is also a reduction in the droplet size between these locations, from plane IV to plane I. For 60° swirler, peak values in droplet size are observed in the peripheral region at all the planes ($z/L_d = 0.333$, 0.433, 0.533, and 0.666) because of the longer recirculation zone.

Entrainment of smaller droplets by the reverse flow near the axis is also evident, especially at larger axial distances. Only for the axial plane (z/L_d) at 0.333 from the injector, the droplet size on the axis is relatively larger; this could possibly be attributed to the proximity of this plane to the injector, where some larger droplets could also be entrained by the reverse flow.

Figure 9 represents the radial variation of SMD for all swirlers at $z/L_d = 0.533$. Decrease in SMD values is observed with increase in vane angle of the swirler. For 45° and 60° swirlers, $z/L_d = 0.533$ lies within recirculation zone, but for 30° swirler, $z/L_d = 0.533$ lies outside the recirculation zone. Hence, smaller droplets are
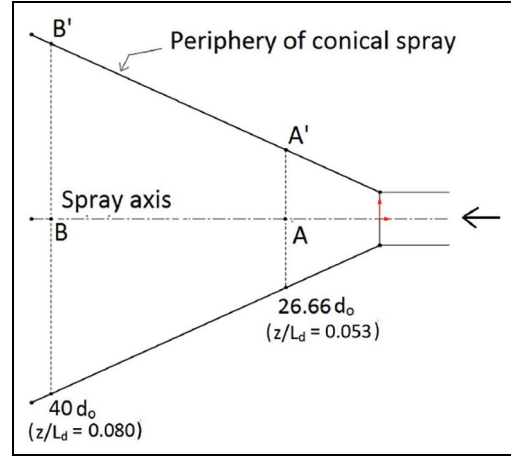
observed close to the axis for 45° and 60° swirlers and larger droplets are observed away from the axis.

Droplet size distribution across the recirculation zone (D1). Droplet size distribution at different axial and radial locations are represented in this section. Figure 10 depicts a schematic of the spray and the axial locations at which droplet distributions are calculated. To understand the droplet breakup process, two points are considered, one on the axis and another at the periphery of conical spray, for two axial positions (A,A′ and B,B′). Figure 11 shows the volume percentage of droplets in various droplet diameter ranges at the mentioned locations. It is observed that due to the presence of recirculation zone, a significant volume fraction of fine droplets is carried along the center line of the spray, especially at the farther axial position (B). Distribution at point A, which is closer to the orifice exit along the center line, shows the presence of large size droplets on the axis as well as at the jet periphery, originating from the initial breakup of ligaments.

Distribution at point B, further downstream of the point A, shows the presence of coarse as well as fine droplets: the coarse droplets originating from the primary breakup and the fine droplets being carried over by the recirculating airflow, after secondary breakup. The contribution of the smaller droplets in the distribution increases significantly along the axis, as seen from the table for location B, in comparison with that for the corresponding peripheral point B′. The peripheral point B′ has a wider distribution of coarse and fine droplets. Along the periphery, at A′ and B′, the size distribution tends to shift toward fine droplets as we move away from the orifice, confirming the secondary breakup of coarse droplets into fine droplets. Away from the injector (B and B′), the droplet distribution becomes multi-modal with multiple peaks over
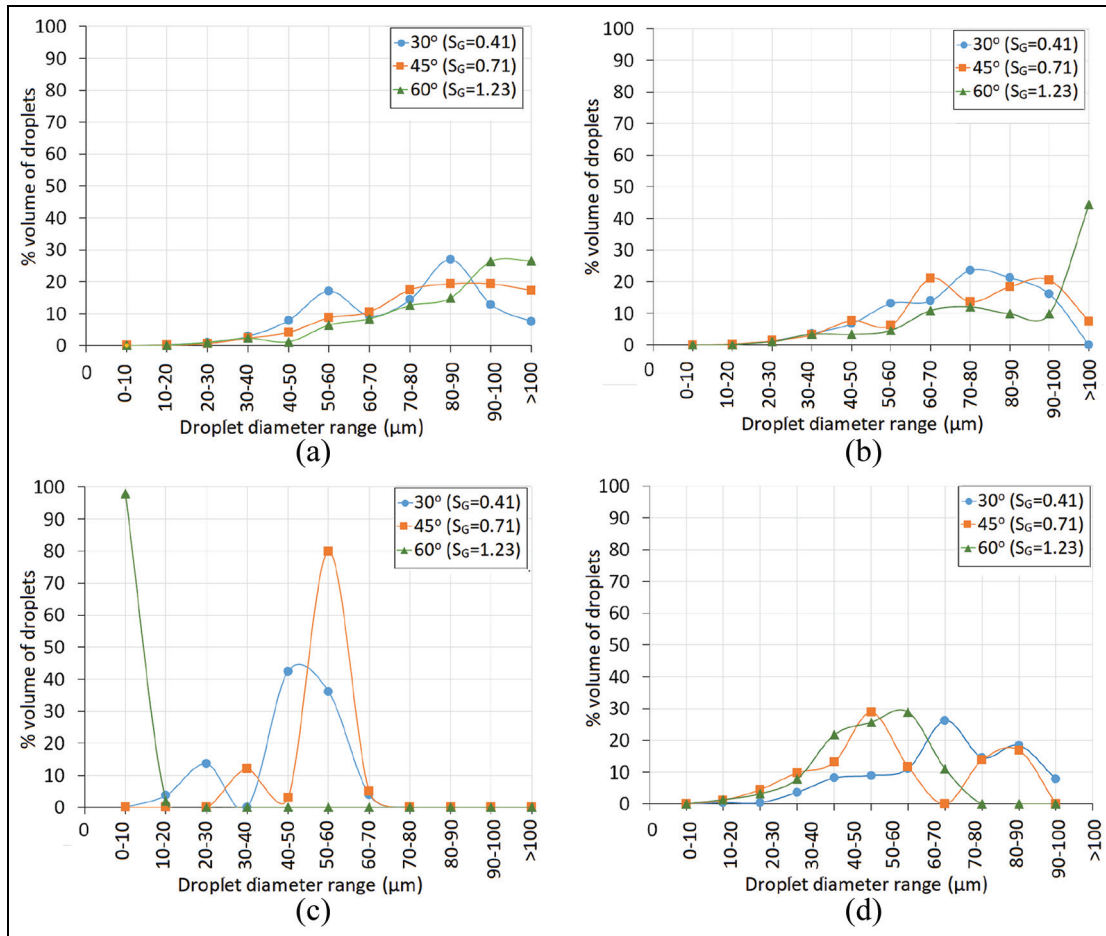
Figure 11. Distribution of spray droplets ($Re_a = 1.35\times10^5$, $Re_l = 7.93\times10^3$, $We^* = 32967$): (a) A, (b) A′, (c) B, and (d) B′.

different size ranges, in general. This can be attributed to concurrent processes such as secondary breakup and the effect of recirculatory flow which entrains fine droplets toward the injector.

Drop size measurement (in-house experimental) and comparison with numerical prediction (D2). Figure 12(a)–(c) represents the radial variation of SMD for 30°, 45°, 60° curved and flat vane swirlers at 40 mm downstream swirler exit.

The discrete symbols represent experimental values and solid or dash lines represent numerical results. Each set of experiment is repeated for five times; the scatter in the data (± 5%) is also shown about the mean value to represent the dispersion in data. The radial variation of SMD is negligible for the 30° swirler due to weak recirculation. For 45° and 60° swirlers, strong recirculation leads to small drops being entrained by the reverse flow near the spray axis. So, the local SMD is small near the axis and high near the periphery of the spray. From Figure 12(a)–(c), it is evident that the SMD value decreases with increase in

Table 7. Comparison between flat and curved vane swirlers.

Properties	60° flat vane swirler	60° curved vane swirler
Maximum reverse velocity (m/s)	4.65	8.94
Pressure loss factor across the swirler	5.59	3.76
Skin friction coefficient at swirler exit	4.68	2.47

vane angle because of the higher swirl strength of the flow. Curved vane swirler results in lower SMD values as compared to a flat vane swirler, for the same airflow rate. This can be attributed to the fact that the swirl air–droplet interactions are superior when curved vane swirler is used instead of a flat vane swirler. Some of the predicted quantities such as maximum reverse velocity, pressure loss factor, and skin friction coefficient value for the flat vane and curved vane swirlers (with blade angle of 60°) are compared in Table 7. It is evident from the comparisons shown in Table 7 that curved vane swirler suffers less losses and hence
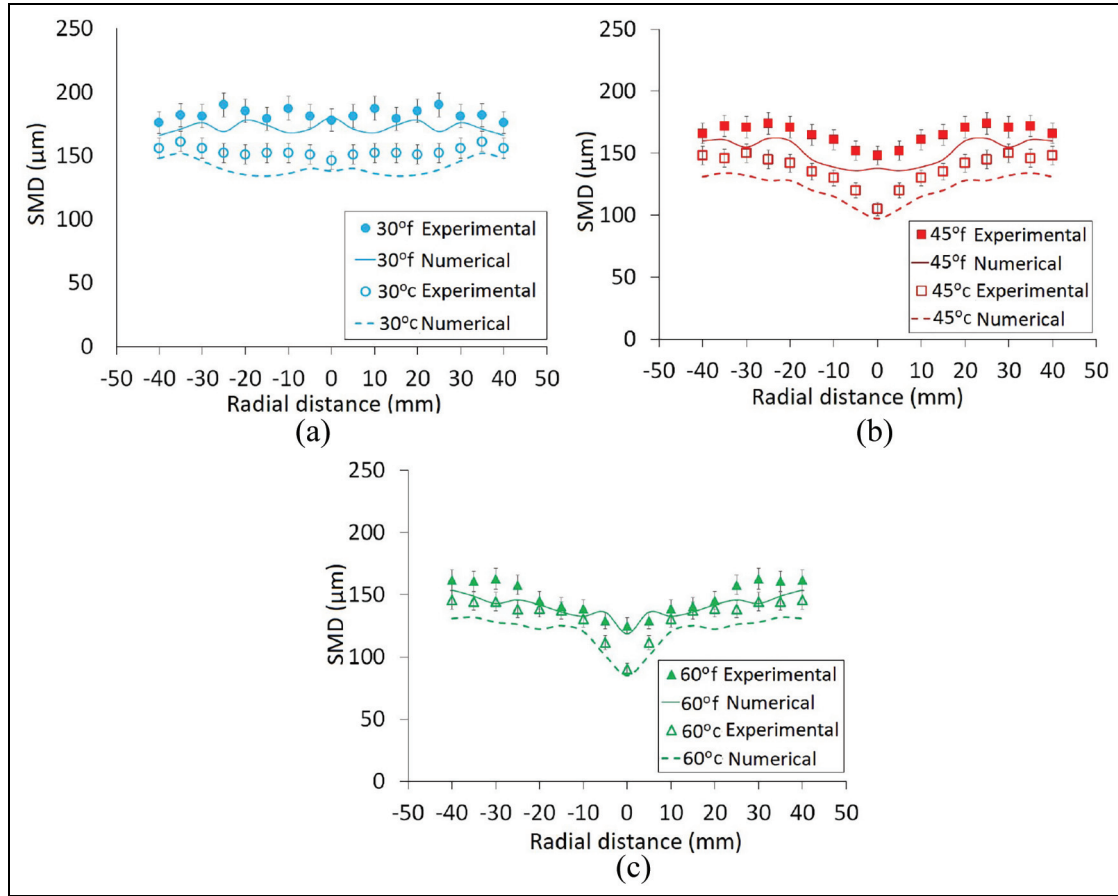
Figure 12. Comparison of predictions for the radial variation of SMD with experimental data ($Re_a = 4.86 \times 10^4$, $Re_l = 2.46 \times 10^4$, $We^* = 4121$): (a) for 30° flat and curved swirlers ($S_G = 0.46$), (b) for 45° flat and curved swirlers ($S_G = 0.46$), and (c) for 60° flat and curved swirlers ($S_G = 0.46$).
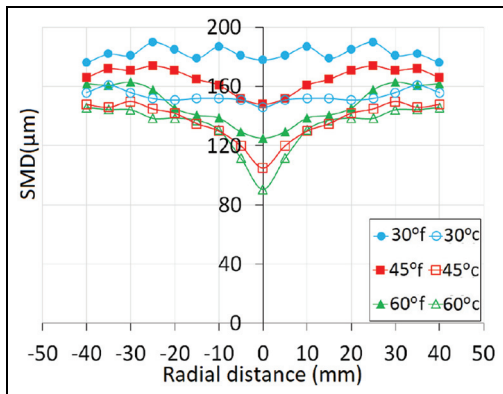

Figure 13. Radial variation of SMD for all swirlers ($Re_a = 4.86 \times 10^4$, $Re_l = 2.46 \times 10^4$, $We^* = 4121$).

provides relatively better performance than a flat vane swirler.

The numerical values closely follow the experimental values, thus validating the spray models used in the present work. The spray cone angle (30°) for the DPM simulation is provided from the average experimental value obtained from high-speed images, since flow inside the injector has not been modeled in this study. The minor differences seen between the numerical and experimental data in Figure 12 could be due some of the simplifying assumptions made for the spray model.

Figure 13 represents the impact of three different swirler configurations on the radial variation of SMD at 40 mm downstream swirler exit. SMD values decrease with increase in vane angle of the swirler, and the use of curved vane swirler results in lower SMD as compared to the flat vane swirler. Increase of vane angle increases the swirl number as given by equation (2) and a higher swirl momentum gives rise to better atomization (i.e. smaller SMD). As regards flat and curved vanes with the same exit vane angle value, a curved vane provides smooth guidance for the airflow from the inlet to the exit of the air swirler. Therefore, pressure drop across the swirler is less for the curved vane swirler, and with less losses, momentum interaction between the airflow and the droplets is enhanced
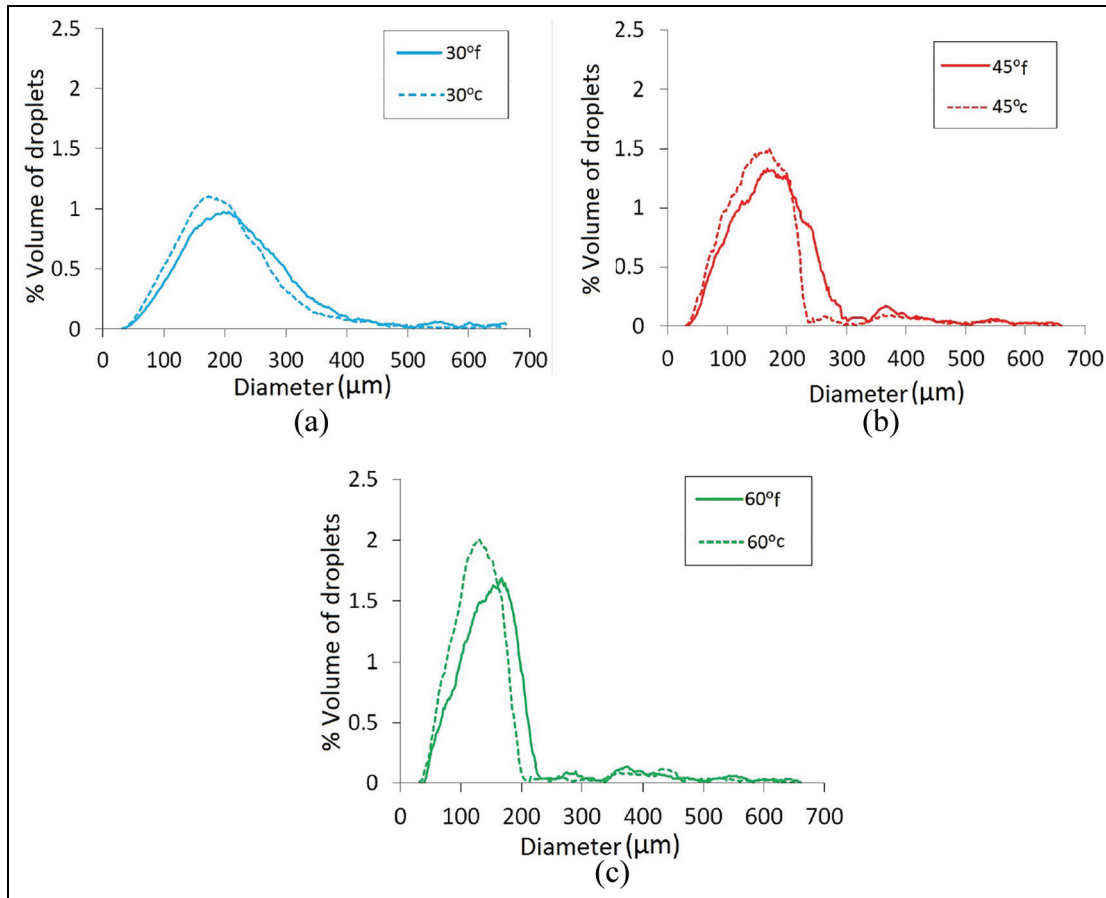
Figure 14. Percentage volume of droplets versus diameter range ($Re_a = 4.86 \times 10^4$, $Re_l = 2.46 \times 10^4$, $We^* = 4121$): (a) for 30° flat and curved swirlers ($S_G = 0.46$) and (b) for 45° flat and curved swirlers ($S_G = 0.80$).

(Table 7). This results in better atomization of the spray in the case of the curved vane swirler.

Figure 14(a)–(c) represents the variation of percentage (%) volume of droplets with droplet size at 40 mm axial location for different swirlers. It is observed that as the vane angle increases, the percentage of droplets lying in the smaller droplet diameter range increases. The peak shifts toward left (finer droplets) by the use of curved vane swirler and the range becomes narrower which shows the uniformity of the droplets.

Conclusion

The interaction between swirl air and spray droplets in a pressure swirl atomizer (simplex atomizer) has been analyzed computationally and experimentally. The numerical predictions for the airflow field, recirculation zone size, and spatial distribution of SMD have been validated with available experimental data. Increase in the swirl angle from 30° to 60° introduces large changes in the magnitude of swirl velocity, recirculation zone (CTRZ) dimensions, turbulence intensity, and the reverse flow velocity magnitude in the recirculation zone. Increase in the number of vanes or variation in airflow rate do not alter the recirculation zone size significantly. However, secondary droplet breakup increases with inlet velocity of the swirl air. The droplet size distribution in the radial direction is significantly modified by the presence of reverse flow in the recirculation zone. Larger drop sizes are observed near the periphery of the spray due to liquid swirl and entrainment of spray droplets by the swirl air in the forward direction. Smaller droplets are observed near the axis due to entrainment by the reverse flow of air. Beyond the recirculation zone, maximum drop size occurs on the axis. Multi-modal droplet size distributions are observed due to the interplay between swirl airflow and liquid spray, especially at higher axial distances and locations close to the axis. A curved vane geometry results in smaller droplet sizes, as compared to those of a flat vane swirler. This can be attributed to the smoother guidance of swirl airflow by the curved vanes. Good agreement is observed between the present experimental data and numerical predictions, for the average droplet size as well as the droplet size distribution. The experimental and numerical results presented

in this work can provide a good understanding of the interactions between spray droplet and swirl air in a gas turbine combustor and pave the way for the design of optimal air swirler.

ORCID iDs

Shraddha Sharma ![iD](https://orcid.org/0000-0001-7429-1187)
Kushal Ghate ![iD](https://orcid.org/0000-0002-9702-8821)
Thirumalachari Sundararajan ![iD](https://orcid.org/0000-0001-9961-355X)
Srikrishna Sahu ![iD](https://orcid.org/0000-0003-2684-5979)

References

1. Syred N and Beer JM. Combustion in swirling flows: a review. *Combust Flame* 1974; 23: 143–201.
2. Gupta AK, Lilley DG and Syred N. *Swirl flows*. Tunbridge Wells: Abacus Press, 1984.
3. Beer JM and Chigier NA. *Combustion aerodynamics*. London: Applied Science Publisher, 1972.
4. Vu BT and Gouldin FC. Flow measurements in a model swirl combustor. *AIAA J* 1982; 20: 642–651.
5. Driscoll JF, Chen RH and Tangirala V. The role of recirculation in improving internal mixing and stability of flames. *AIAA J* 1987; 87: 306–325.
6. Reddy AP, Sujith RI and Chakravarthy SR. Swirler flow field characteristics in a sudden expansion combustor geometry. *J Propul Power* 2006; 22: 800–808.
7. Raj TK and Ganesan V. Experimental study of recirculating flows induced by vane swirler. *Ind J Eng Mater Sci* 2009; 16: 14–22.
8. Dang X, Zhao J, Rong X, et al. Experimental investigation on effects of swirl number on aerodynamic characteristics of the combustor. *J Aerosp Power* 2011; 26: 21–27.
9. Kilik E. *The influence of swirler design parameters on the aerodynamics of downstream recirculation region*. PhD Thesis, Cranfield Institute of Technology, Cranfield, 1976.
10. Muthuselvan G, Ghate KD, Rao MS, et al. Experimental study of spray breakup phenomena in small-scale simplex atomizers with and without air swirl. *Atomization Sprays* 2018; 28: 299–320.
11. Khandelwal B, Lili D and Sethi V. Design and study on performance of axial swirler for annular combustor by changing different design parameters. *J. Energy Inst* 2014; 87: 372–382.
12. Yilmaz I. Effect of swirl number on combustion characteristics in a natural gas diffusion flame. *J Energy Res Technol* 2013; 135: 042204.
13. Khavkin YI. *Theory and practice of swirl atomizers*. London: CRC Press, 2003.
14. Archer S and Gupta AK. Effect of swirl and combustion on flow dynamics in lean direct injection gas turbine combustion. In: *Proceedings of the 41st AIAA aerospace sciences meeting*, Reno, NV, 6–9 January 2003. Reston, VA: AIAA.
15. Dunand A, Carreau JL and Roger F. Liquid jet breakup and atomization by annular swirling gas jet. *Atomization Sprays* 2005; 15: 223–247.
16. Sanadi D, Rajamanickam K and Basu S. Analysis of hollow-cone spray injected in an unconfined, isothermal, coannular swirling jet environment. *Atomization Sprays* 2017; 27: 7–29.
17. De La Rosa AB, Wang G and Bachalo WD. The effect of swirl on the velocity and turbulence fields of a liquid spray. *J Eng Gas Turb Power* 1992; 114: 72–81.
18. Hadef R and Lenze B. Effects of co-and counter-swirl on the droplet characteristics in a spray flame. *Chem Eng Proces* 2008; 47: 2209–2217.
19. Rajamanickam K and Basu S. Insights into the dynamics of spray–swirl interactions. *J Fluid Mech* 2017; 810: 82–126.
20. Shih TH, Liou WW, Shabbir A, et al. A New K-eddy viscosity model for high Reynolds number turbulent flows. *Comput Fluids* 1995; 24: 227–238.
21. Schmidt DP, Nouar I, Senecal PK, et al. Pressure-swirl atomization in the near field. SAE technical paper 1999-01-0496, 1999.
22. Taylor GI. The shape and acceleration of a drop in a high speed air stream. In: Batchelor GK (ed.) *The scientific papers of G. I. Taylor*, vol. 3. Cambridge: Cambridge University Press, 1963, pp.457–464.
23. Haider A and Levenspiel O. Drag coefficient and terminal velocity of spherical and nonspherical particles. *Powder Technol* 1989; 58: 63–70.
24. Coghe A, Solero G and Scribano G. Recirculation phenomena in a natural gas swirl combustor. *Exp Therm Fluid Sci* 2004; 28: 709–714.
25. Lefebvre AH. *Atomization and sprays*. 1st ed. Boca Raton, FL: CRC Press and Taylor and Francis Group, 1989.